Geophysical Research Letters

RESEARCH LETTER
10.1029/2024GL112433

Unexpected Warming From Land Radiative Management

Yu Cheng[1] and Kaighin A. McColl[1,2]

[1]Department of Earth and Planetary Sciences, Harvard University, Cambridge, MA, USA, [2]School of Engineering and Applied Sciences, Harvard University, Cambridge, MA, USA

Key Points:

- Land radiative management (LRM) causes temperatures to unexpectedly increase in surrounding regions
- LRM decreases precipitation over its immediate surroundings, which dries the land surface and increases temperatures
- The unilateral adoption of LRM by affluent regions will exacerbate heat inequality between wealthy and poor neighborhoods

Supporting Information:

Supporting Information may be found in the online version of this article.

Correspondence to:

K. A. McColl,
kmccoll@seas.harvard.edu

Citation:

Cheng, Y., & McColl, K. A. (2024). Unexpected warming from land radiative management. *Geophysical Research Letters*, *51*, e2024GL112433. https://doi.org/10.1029/2024GL112433

Received 9 SEP 2024
Accepted 16 OCT 2024

Abstract "Land radiative management" (LRM)—deliberately increasing surface albedo to decrease temperatures—has been proposed as a form of geoengineering to mitigate the effects of regional warming. Here, we show that, contrary to expectations, LRM causes temperatures to increase in surrounding regions. The basic reason for the increase is unintended impacts on precipitation. Precipitation is suppressed over the LRM region, but this effect also extends to nearby areas unprotected by LRM. The reduction in precipitation and soil moisture in these regions leads to higher temperatures than would be expected in the absence of LRM. The resulting warming outside the LRM region is comparable to the cooling achieved inside it. This implies that, if wealthy regions unilaterally adopt LRM to cool, their neighbors may experience warming, worsening heat inequality.

Plain Language Summary Land radiative management (LRM), which involves artificially increasing Earth's surface albedo to mitigate regional warming, has been recognized by the Intergovernmental Panel on Climate Change as a potential solution to combat the adverse effects of climate change. Examples of LRM approaches include the adoption of white roofs and pavements. Our study challenges conventional wisdom by demonstrating that LRM can actually cause temperatures to increase, rather than decrease as intended, due to its unintended impacts on rainfall. LRM suppresses rainfall in surrounding regions, causing them to experience higher temperatures than they would in the absence of LRM. The implications of our findings are significant, as the unilateral adoption of LRM by affluent regions will exacerbate heat inequality between wealthy and poor neighborhoods.

1. Introduction

Land radiative management (LRM) aims to reduce temperatures at local and regional scales by artificially increasing surface albedo, resulting in less shortwave radiation absorption at the land surface (Seneviratne et al., 2018). Approaches to LRM include white roofs (Li et al., 2014; Mackey et al., 2012; Sharma et al., 2016; Vahmani et al., 2016) and pavements (Erell et al., 2014; Taleghani et al., 2016), no-till farming (Davin et al., 2014; Hirsch et al., 2017; Seneviratne et al., 2018; Wilhelm et al., 2015), and desert albedo enhancement (Irvine et al., 2011). While LRM is currently limited to small scales, it is conceivable that LRM will approach mesoscales ($O(10\,\mathrm{km})$) in future, and has attracted growing interest (Jia et al., 2019; Seneviratne et al., 2018).

Previous modeling studies have found that LRM causes reductions in both mean (Irvine et al., 2011; Seneviratne et al., 2018) and extreme temperatures (Hirsch et al., 2017; Wilhelm et al., 2015). Those studies used general circulation models (GCMs), which neglect important storm formation mechanisms that can be significant at the smaller scales most relevant to LRM. While some regional climate model simulations have been performed at sufficiently fine resolutions to resolve mesoscale circulations (Fallmann et al., 2013; Li et al., 2014; Lynn et al., 2009; Synnefa et al., 2008), the computational expense has precluded the analysis of long simulations necessary to distinguish rainfall signal from noise. Other studies simulate the temperature and precipitation response to changes in albedo due, for example, to deforestation (Taylor et al., 2022; Wang et al., 2000). However, deforestation is, at best, an imperfect analog for LRM, since it modifies not just surface albedo, but also roughness and other factors that generate their own confounding impacts on temperature and precipitation (Cheng & McColl, 2023).

Here, we use mesoscale convection-permitting simulations and a simple theory to show that LRM causes temperatures to unexpectedly increase in surrounding regions. The fundamental reason for this surprising result is mesoscale storm formation mechanisms (Baidya Roy & Avissar, 2002; Cheng et al., 2023; Wang et al., 2000) that have been neglected in previous LRM studies.

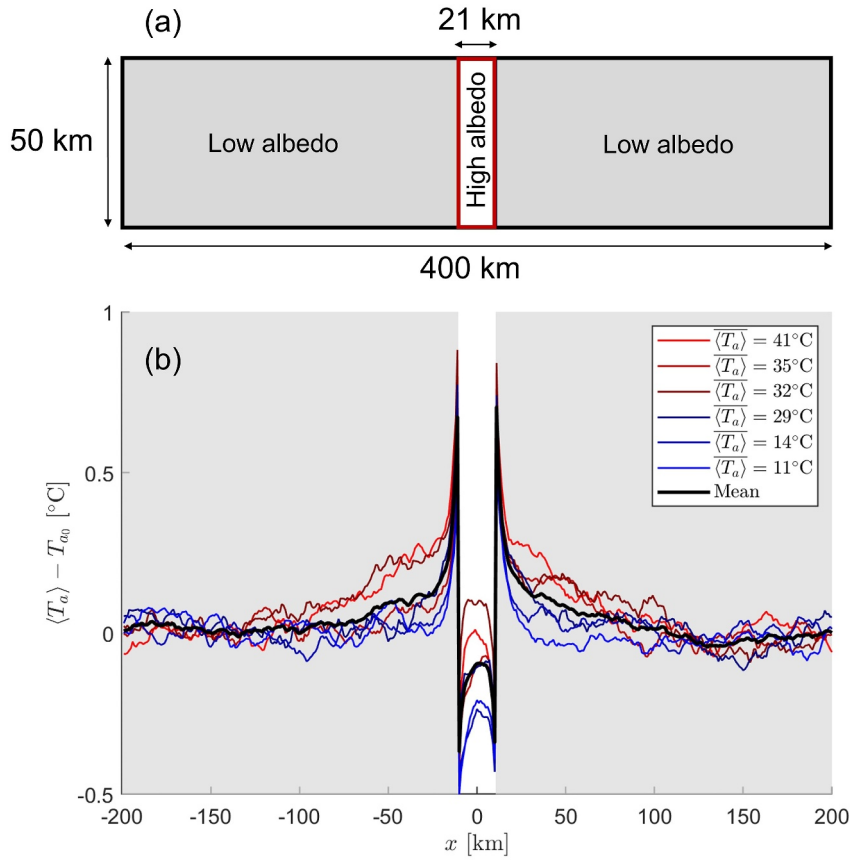

Figure 1. LRM causes warming in mesoscale simulations. (a) Schematic of the simulated domain. The size of the domain is 400 km × 50 km, and the width of the high-albedo rectangle denoting the LRM region at the center of the domain is 21 km. The schematic is not to scale. (b) Near-surface air temperature anomaly $\overline{\langle T_a \rangle} - T_{a_0}$, where T_a is near-surface air temperature (2 m above the surface) averaged between 6 a.m. and 6 p.m. from the experiment A_RCE (Table S1 in Supporting Information S1), T_{a_0} refers to average near-surface air temperature far from the LRM region, $\langle\rangle$ denotes long-term temporal averaging, and $\overline{\ }$ denotes spatial averaging. Each simulation is denoted by its mean daytime temperature in the legend. The thick black lines denote the mean values across simulations. See "Mesoscale convection permitting simulations" in Supporting Information S1 for further details.

2. LRM Causes Warming in Mesoscale Simulations

We perform idealized simulations of an LRM region using mesoscale convection-permitting models (Khairoutdinov & Randall, 2003). Rather than using a complex urban canopy model, or focusing on one specific location, we prescribe a high surface albedo anomaly in an otherwise homogeneous environment. The idealized nature of these simulations permits a clearer diagnosis of relevant mechanisms, and thus makes our findings more generalizable. A high surface albedo anomaly (21 km × 50 km in horizontal x and y directions, respectively) is prescribed in the middle of an otherwise uniform domain (400 km × 50 km in x and y directions, respectively) as shown in Figure 1a. The prescribed visible albedo of the land surface in the LRM region and the surrounding background region are 0.1425 and 0.0356, respectively, comparable to the albedo change caused by cropland management in Davin et al. (2014). Simulations are conducted over a wide range of conditions, with domain-averaged near-surface air temperatures varying between 11 °C and 41 °C during the day (as detailed in Tables S1 and S2, and Figure S2 in Supporting Information S1). For simulations presented in Figures 1 and 2, only the latitude of the domain center and thus top-of-atmosphere solar radiation is varied (Table S2 in Supporting Information S1). Because our simulations are of idealized land regions, the resulting climates span a much wider range than the corresponding climates of Earth at these latitudes. Further details on the numerical simulations are provided in Supporting Information S1 (Cheng et al., 2021; Cioni & Hohenegger, 2017; ECMWF, 2016; Khairoutdinov & Randall, 2003; Kiehl et al., 1998; Lee & Khairoutdinov, 2015; Monin & Obukhov, 1954). We

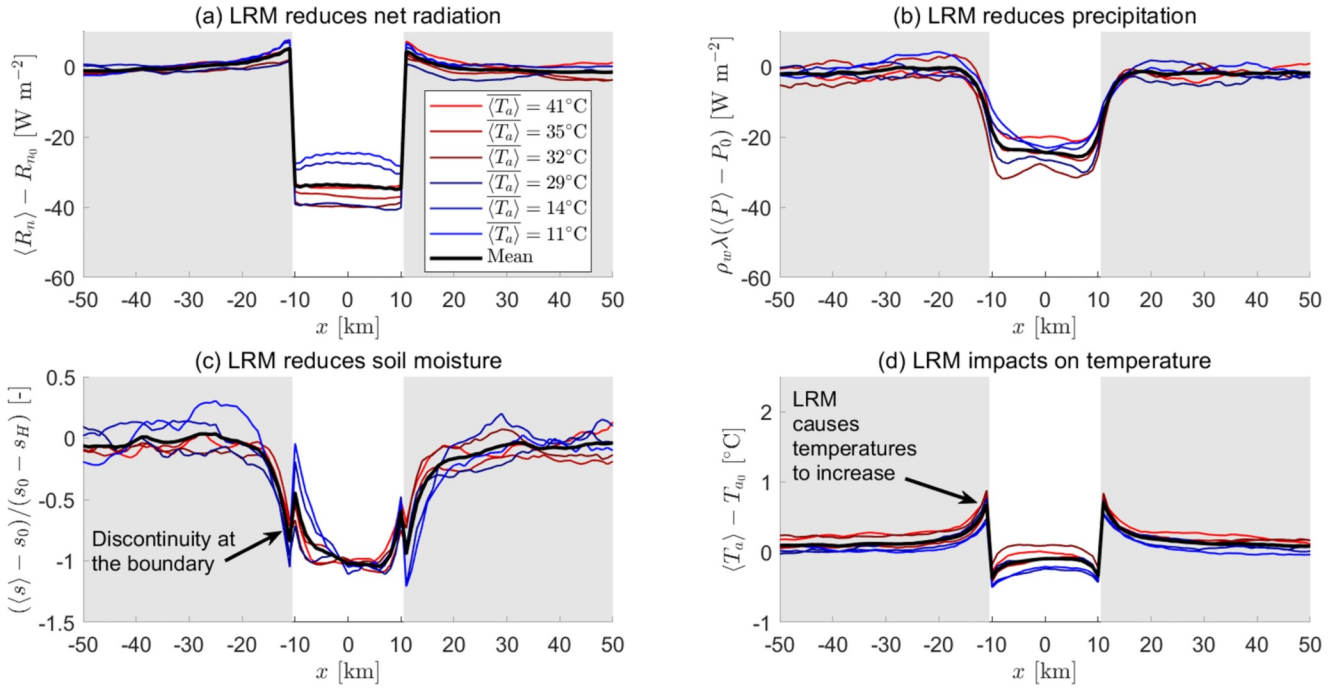

Figure 2. Simulated changes in net radiation, precipitation and soil moisture associated with LRM warming. (a) LRM reduces net radiation (R_n). (b) LRM reduces precipitation (P). ρ_w is the density of water, and λ is the latent heat of vapourization. (c) LRM reduces soil moisture, and causes a discontinuity to arise at the boundary of the LRM region. The normalized change in soil saturation $\frac{\langle s \rangle - s_0}{s_0 - s_H}$ is shown. (d) LRM changes temperature, causing it to cool inside the LRM region, and rise immediately outside it. The terms with an "H" subscript correspond to values in the LRM region, and terms with a "0" subscript correspond to values far from the LRM region. The thick black lines denote the mean values across simulations. All quantities are averaged between 6 a.m. and 6 p.m.

examine the responses of both surface (T_s) and near-surface air temperatures (T_a), but focus on near-surface air temperatures since they are most directly relevant to human health (Chakraborty et al., 2022).

Inside the LRM region, the near-surface air temperature is generally lower than that over the surrounding region (Figure 1b). However, unexpected warming occurs in the immediate surroundings of the LRM region (Figure 1b). The warming is comparable to (and, typically, greater than) the cooling achieved inside the LRM region: for the experiments shown in Figure 1b, the warming is between 110% and 400% of the maximum cooling achieved inside the LRM region. A qualitatively similar response is observed in land surface temperatures (Figure S3 in Supporting Information S1).

The observed warming outside the LRM region is robust to varying different aspects of the simulations. The warming persists in additional simulations in which a mean wind was imposed parallel to the land surface (Figure S4 in Supporting Information S1, experiment A_RCE_wind), although the warming location shifts downwind. The warming is also not especially sensitive to imposed atmospheric dynamics. Rather than imposing radiative-convective equilibrium (RCE, as discussed in previous studies (Held et al., 1993; Manabe & Strickler, 1964; Miyawaki et al., 2022)), we also ran simulations that invoke the weak temperature gradient (WTG, Figure S5 in Supporting Information S1, experiment A_WTG) approximation (Sobel et al., 2001), which permits domain-averaged atmospheric subsidence or uplift and has been applied extensively over a limited domain to model the interaction between convection and large-scale forcing over a tropical land surface (Abbott & Cronin, 2021, 2023; Cheng & McColl, 2023; Raymond & Zeng, 2005). In addition, the warming remains in simulations in which the LRM region is much smaller (Figure S6 in Supporting Information S1, experiment B_WTG). Finally, we performed control simulations (A_RCE_ctl) with spatially uniform surface albedo identical to the domain-averaged surface albedo in the experiment A_RCE, and used mean temperatures from these simulations ($\overline{\langle T_{a,\mathrm{ctl}} \rangle}$) as references in estimating temperature anomalies, rather than the mean temperature far from the LRM region in the original simulations (T_{a_0}). The warming persists in these simulations, too (Figures S7 and S8 in Supporting Information S1).

3. Changes in Rainfall Cause LRM Warming

The observed warming outside the LRM region is surprising, given the goal of LRM is to reduce temperatures. To our knowledge, warming from LRM has not been previously reported. Why does LRM cause warming in surrounding regions?

Increasing surface albedo has two impacts on a region. First, it reduces surface temperatures by reflecting a greater fraction of solar radiation, as intended. Figure 2a shows surface net radiation (R_n) is substantially reduced in the LRM region in our simulations, relative to surface net radiation in surrounding regions (R_{n_0}). Surface net radiation is highest just outside the LRM region, but the difference with surrounding regions is ultimately small. This peak in net radiation is caused by changes in cloud cover, discussed in the next paragraph. As we will see, it is not the main cause of warming outside the LRM region.

Second, it causes mesoscale circulations to form at the boundaries of the LRM region, which suppress precipitation inside the LRM region. Figure 2b shows that precipitation (P) is substantially reduced in the simulated LRM region, relative to precipitation in surrounding regions (P_0). The heating differential between the LRM region and its surroundings causes a thermally direct mesoscale circulation to form (Cheng et al., 2023; Physick & Tapper, 1990), analogous to a land-sea breeze (where the LRM region is the "sea" in this analogy). The mesoscale circulation causes subsidence in the LRM region, which suppresses precipitation and cloud cover. It also causes air to rise outside the LRM region, which enhances precipitation and cloud cover. The extra precipitation generated outside the LRM region is spread thinly over a larger region, and is not obviously distinguishable from internal variability in our simulations.

Reductions in precipitation dry soils in the LRM region, whereas reductions in net radiation moisten it by reducing evaporative demand. On balance, soils dry in response to LRM in our simulations (Figure 2c). In addition, a discontinuity in the soil moisture profile arises at the boundaries of the LRM region. This robust feature is observed across a wide range of simulations.

We use a parsimonious conceptual model to explain these results. The conceptual model takes profiles of net radiation (Figure 3a) and precipitation (Figure 3b) as inputs. Based on observed profiles, we use an expression based on a logistic function to represent these profiles. The profiles smoothly connect the relatively lower values of surface net radiation and precipitation in the LRM region with corresponding higher values in the surrounding environment (Equations S1 and S2 in Supporting Information S1). These profiles are used to estimate a profile of soil saturation (Figure 3c) using a recent theory (Stahl & McColl, 2022), which is then used to predict a temperature profile (Figure 3d) using a simplified model of the atmospheric boundary layer (Garratt, 1992; Porporato, 2009; Tennekes, 1973). Full details of the conceptual model are provided in Supporting Information S1 (Brutsaert & Sugita, 1992; Driedonks, 1982; Gentine et al., 2007; Koster & Mahanama, 2012; Koster et al., 2009; Seneviratne et al., 2010; Stahl & McColl, 2022).

We first use the conceptual model to consider a naive example, in which there is no unexpected warming outside the LRM region. In this example, it is assumed that turbulent mixing and advection in the atmosphere are negligible. Reductions in surface net radiation and precipitation are confined to the LRM region itself (Figures 3a and 3b, black lines). The net effect is a reduction in soil moisture inside the LRM region (Figure 3c, black line), which reduces evaporative cooling and increases temperatures, all else being equal. This conceptual model predicts that the net effect of decreases in surface net radiation and in evaporative cooling is a reduction in surface temperatures (Figure 3d, black line), with no anomalous warming outside the LRM region. Since our simulations show anomalous warming outside the LRM region, something is missing from this explanation.

The key missing mechanism is turbulent mixing and advection in the atmosphere. Unlike the land surface, the atmosphere is a turbulent, well-mixed fluid. This means that, at the boundary of the LRM region, the precipitation anomaly caused by LRM varies smoothly over some non-zero length scale L_P (Figure 3b, red line), where L_P is the length scale over which precipitation P transitions from lower values in the LRM region to higher values outside the LRM region. In contrast, surface net radiation is largely determined by land surface properties and, thus, is discontinuous at the LRM boundary, implying $L_{R_n} \approx 0$ (Figure 3a). This spreads anomalously lower soil moisture *outside* the LRM region (Figure 3b, red solid line), creating a region that experiences the downsides of LRM (reduced evaporative cooling) without its benefits (reduced absorption of

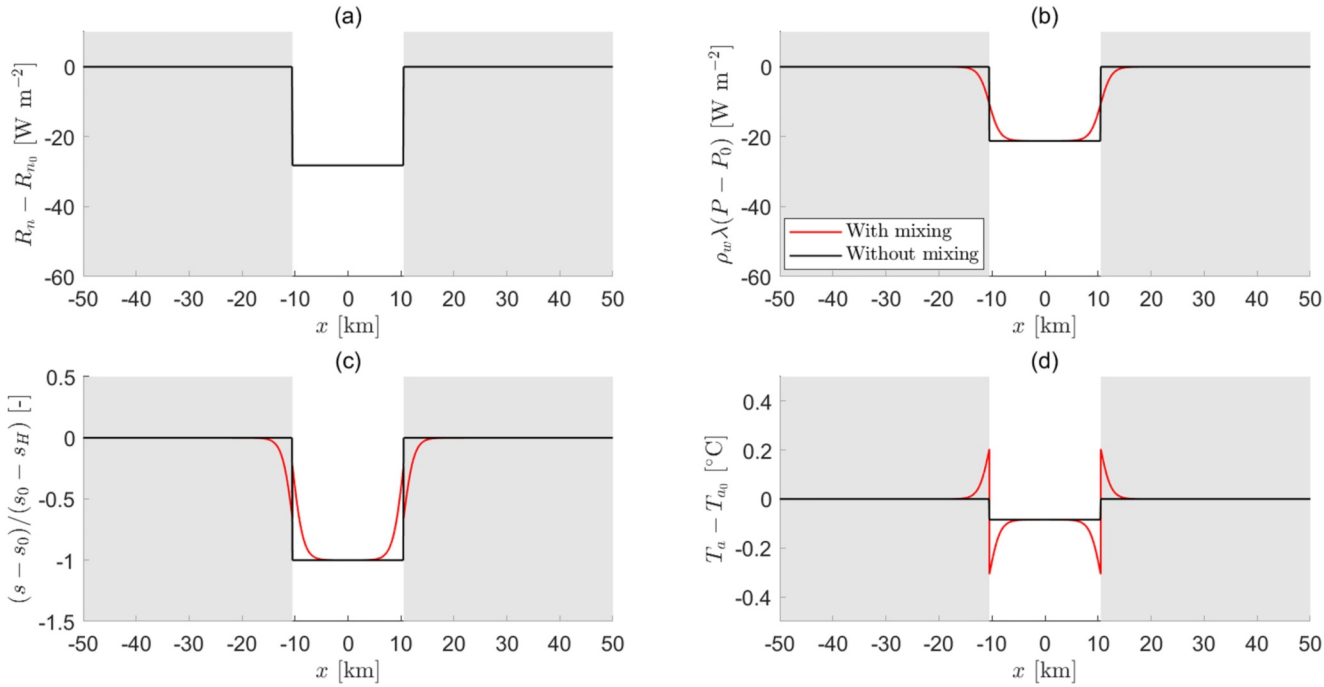

Figure 3. A conceptual model explains the observed warming outside the LRM region. Full details of the conceptual model are provided in Supporting Information S1. Here, the conceptual model is applied to the simulation A_RCE, $\overline{\langle T_a \rangle} = 14$ °C. (a) Prescribed net radiation anomaly profile (Equation S2 in Supporting Information S1, $L_{R_n} = 0$ km). (b) Prescribed precipitation anomaly profile (Equation S1 in Supporting Information S1) with atmospheric mixing and advection included (red line, $L_P = 1$ km) and excluded (black line, $L_P = 0$ km). (c) Predicted soil moisture anomaly (Equation S4 in Supporting Information S1) using prescribed profiles of net radiation in (a) and precipitation in (b). (d) Predicted near-surface air temperature anomaly using Equation S16 in Supporting Information S1 (with parameters $\gamma_\theta = 8 \times 10^{-3}$ K m^{-1}, $\beta = 0.2$; other parameters obtained by fitting to the simulation A_RCE, $\overline{\langle T_a \rangle} = 14$ °C). Note that the y-axis limits in (d) differ from those in Figure 2d.

radiation). This is the ultimate cause of the anomalous warming outside the LRM region in our simulations (Figure 3d, red solid line). The same mechanism also creates a region just inside the LRM boundary that experiences both increased evaporative cooling *and* reduced absorption of radiation, explaining why the greatest cooling from LRM occurs near its boundaries. Finally, including turbulent mixing and advection in the conceptual model is sufficient to reproduce the discontinuity in the soil moisture profile at the LRM boundary observed in simulations (Figure 3c).

To further test this explanation, we conducted an additional simulation in which soil moisture is fixed to be spatially uniform at its domain-averaged value (A_RCE_fixsoil, Table S1 in Supporting Information S1). In this simulation, the proposed mechanism is switched off. Some warming still occurs outside the LRM boundary in this simulation due to changes in cloud cover caused by mesoscale circulations. However, its magnitude is relatively small: less than 24% of the maximum cooling achieved within the LRM region (Figure S9 in Supporting Information S1), compared with 110% in the corresponding simulation with interactive soil moisture (Figure 2d). Thus, our explanation in terms of soil moisture appears to be the dominant reason for the anomalous warming. The conceptual model is sufficient to qualitatively reproduce the observed warming profile, but somewhat underestimates the absolute temperature values. It also does not explain why peak warming outside the LRM region typically exceeds peak cooling inside it. This is likely due, in part, to its neglect of cloud effects. While this could be addressed by adding further complexity to the conceptual model, it does not seem essential in qualitatively explaining why the unexpected warming arises.

In summary, rainfall is suppressed over both the LRM region and its immediate surroundings, drying the land surface and increasing temperatures. While the LRM region benefits from reflective cooling that more than offsets this warming, the surrounding regions do not. The net effect is warming outside the LRM region.

4. Discussion

4.1. Relation to Previous Studies

There is a vast prior literature on surface albedo impacts on temperature and rainfall (Charney et al., 1977; Physick & Tapper, 1990; Taylor et al., 2022; Wang et al., 2000). Yet, as reviewed in Cheng et al. (2023), much of that is not directly relevant to LRM, for several reasons. First, LRM would be implemented at mesoscales (O(1–10 km)), which are too small to be resolved in many prior studies based on GCMs (Charney et al., 1977). Second, while some prior studies simulate mesoscale albedo modification, they do not consider changes in albedo independently of other changes. For example, studies of deforestation impacts on temperature and precipitation modify not only surface albedo, but also roughness and other factors that are not directly relevant to LRM (Taylor et al., 2022; Wang et al., 2000), and which also cause changes in temperature and precipitation (Cheng & McColl, 2023). Third, some studies simulate the transient temperature and precipitation response, but not the long-term equilibrium response (Physick & Tapper, 1990; Wang et al., 2000). This response is most relevant to LRM, which involves a permanent modification to the landscape.

Other studies have focused specifically on LRM (Davin et al., 2014; Irvine et al., 2011; Wilhelm et al., 2015). To identify the warming mechanism, there are three basic requirements for any simulation: (a) sufficiently high spatial resolution; (b) sufficiently large domain size; and (c) sufficiently long temporal coverage. No prior study satisfies all three of these requirements. First, many previous simulations (Davin et al., 2014; Hirsch et al., 2017; Irvine et al., 2011; Wilhelm et al., 2015) are not conducted at a sufficiently fine spatial resolution to resolve the region experiencing higher temperatures around the LRM region. For example, the horizontal resolution in regional climate models (Davin et al., 2014) and GCMs (Irvine et al., 2011; Wilhelm et al., 2015) are O(10 km) and O(100 km), respectively. In our simulations, the region experiencing warming is O(1 km) in size. This problem is particularly acute for GCMs, which are run at such coarse resolutions that they typically do not even resolve the mesoscale circulations that are essential to the mechanism identified here.

Second, the size of the simulated domain in some prior studies is too small. Mesoscale circulations arise over land surface heterogeneities on scales of O(1–10 km) (Baidya Roy et al., 2003; Patton et al., 2005; Sakaguchi et al., 2022; Tian et al., 2022). While some prior simulations have been conducted at sufficiently high spatial resolution, the size of the simulated domain is too small to produce mesoscale circulations (Alchapar et al., 2017; Middel et al., 2015; Taleghani et al., 2016).

Third, the simulations in some prior studies do not span a sufficiently long time period. Since precipitation exhibits significant internal variability (Lehner & Deser, 2023), considerable temporal averaging is required to identify a statistically meaningful signal. Our simulations were typically run for 1,000 days to address this issue. In contrast, relevant prior simulations often only span a single day, and never more than a few months (Fallmann et al., 2013; Gilabert et al., 2021; Jacobs et al., 2018; Li et al., 2014; Lynn et al., 2009; Sharma et al., 2016; Synnefa et al., 2008; Vahmani et al., 2016).

Cheng et al. (2023) speculated that mesoscale circulations caused by LRM could cool surrounding regions, which might appear to contradict this study's main finding. However, there is no contradiction. This study focuses on a small but significant region just outside the LRM region, in which precipitation and soil moisture are reduced with respect to surrounding regions, which ultimately causes warming in that region. In contrast, Cheng et al. (2023) focused on the average response over a much larger region. While precipitation and soil moisture decrease just outside the LRM region, that does not preclude them from increasing when averaged over the larger surrounding region. Since the changes in precipitation, soil moisture and temperature averaged over this larger area are smaller than those near the LRM boundary, they are not distinguishable from internal variability in our simulations.

4.2. Limitations

Other aspects of urban environments can cause mesoscale circulations to form, which could, in principle, counteract the mechanism proposed here. For example, Cheng and McColl (2023) found that rough surfaces, such as cities, can generate mesoscale circulations and attract rainfall. If the LRM region was systematically rougher than its surroundings—for example, if an entire city was subjected to LRM, and surrounded by farmland—this may counteract the reduction in precipitation found here, and potentially eliminate temperature increases outside the LRM region. However, if the LRM region is just one neighborhood in a larger city, this mechanism is unlikely

to be significant, since the difference in roughness between urban neighborhoods is much smaller than that between urban and rural landscapes.

Our proposed mechanism will only hold in regions where evaporation is sufficiently sensitive to soil moisture. Its effects may be less pronounced in especially cold or wet regions where sensitivity is low. However, the mechanism is clearly evident in our simulations, which span a wide range of climates. Similarly, our proposed mechanism requires that soil moisture is sensitive to precipitation. This sensitivity may be somewhat lower in urban areas, where some fraction of accumulated precipitation flows over paved surfaces into drainage systems rather than soil reservoirs. Future studies should investigate the magnitude of these impacts.

We cannot currently test this mechanism using observations because LRM does not yet exist at mesoscales. Natural experiments are also not available. While it might appear, for example, that the gradient between a forest and grassland, or between a city and farmland, provides a natural albedo gradient, both cases are confounded by other differences (in roughness and vegetation) that strongly impact the heating differential between the two regions (Cheng & McColl, 2023). Nevertheless, the mechanism identified here is understandable in terms of basic physical arguments, and is robust to substantial variations in the details of the simulation.

4.3. Implications

Both high-resolution simulations and simple theory show that LRM will cause temperatures to unexpectedly increase in surrounding regions. The region affected is small (O(1 km)) but significant, with potential to impact many thousands of people in urban areas. For example, if LRM is applied to a 10 km × 10 km region, and warming occurs in a 1 km wide region just outside the LRM boundaries, the resulting region experiencing warming will be 44 km^2. For a population density equivalent to San Francisco's, this would imply roughly 300,000 people would be subject to warming caused by LRM.

How does the size of the LRM-protected region impact the results? There must be some minimum size at which LRM will not impact rainfall, resulting in no warming of surrounding regions. We speculate that this size corresponds to the size for which mesoscale circulations start to form around a land surface anomaly (O(1–10 km)) (Baidya Roy et al., 2003; Patton et al., 2005). Future studies should further investigate this. On the other hand, the unintended warming occurs in a thin band around the sides of the LRM-protected region with a width that scales with L_P. If we speculate that L_P does not change much as the LRM-protected region grows larger, then the size of the impacted region will be mainly a function of the length of the boundary of the LRM-protected region. Since the surface-to-volume ratio is larger for smaller volumes, we speculate that the relative benefit of LRM schemes will be lower for smaller schemes, since relatively larger areas will be exposed to higher temperatures. A back-of-the-envelope calculation illustrates this point. Consider a square LRM domain with side lengths Λ, which cools the area inside its boundaries $\left(\Lambda^2\right)$ and warms the region just outside its boundaries with area $4L_P(\Lambda + L_P)$. Assuming the same population density inside and outside the LRM region, more people experience cooling than warming when $\Lambda^2 > 4L_P(\Lambda + L_P)$. Using the quadratic formula, this requirement simplifies to $\Lambda > 2(1 + \sqrt{2})L_P \approx 5L_P$. Thus, for $L_P \approx 1$ km, as in our simulations, this implies that an LRM region should be at least 5 km × 5 km in size simply to ensure that more people experience cooling than warming. In summary, these arguments suggest the ratio of population warmed to population cooled is lowest for very small schemes ($\ll$1 km, for which LRM does not impact rainfall) and very large schemes ($\gg$10 km). This implies that progressive construction of LRM regions from smaller to larger scales may result in extended periods in which more people suffer from higher temperatures than benefit from cooler temperatures.

If the cost of LRM results in it primarily being implemented in wealthier neighborhoods, the mechanism we identify here would not only worsen heat inequality (Chakraborty et al., 2023; Hsu et al., 2021), but worsen conditions for poorer neighbors in absolute terms. It is theoretically possible that heat inequality could increase even though heat stress declines everywhere in absolute terms (e.g., if heat stress declined to a greater extent in wealthier regions than in poorer regions). Here, however, LRM leads to higher temperatures in neighborhoods bordering the LRM region; not just in *relative* terms, but in *absolute* terms.

This study has focused on diagnosing and understanding the problem of unexpected warming caused by LRM. While possible solutions to this problem are deferred to future studies, we briefly speculate on one possible option. Our theory suggests that designing the LRM scheme in such a way that $L_{R_n} \approx L_P$ would effectively

mitigate the warming. This would require introducing a smaller gradient in albedo around the boundary of the LRM scheme. There are at least three challenges to doing this. First, designing and maintaining such a gradient is more logistically difficult. Second, the length scale L_P for a given LRM geometry and location is unknown a priori. Third, the presence of a mean wind will shift the region experiencing warming, and the location of the region will vary with the direction of the wind, whereas any engineered gradient would be static. All of these challenges require further study.

Conflict of Interest

The authors declare no conflicts of interest relevant to this study.

Data Availability Statement

The data set used for this study is available for public access at the Harvard Dataverse via Cheng and McColl (2024).

Acknowledgments
K.A.M. acknowledges funding from NSF Grant AGS-2129576 and a Sloan Research Fellowship. We thank Marat Khairoutdinov for providing SAM and the land model SLM. The computations in this paper were run on the FASRC Cannon cluster supported by the FAS Division of Science Research Computing Group at Harvard University.

References

Abbott, T. H., & Cronin, T. W. (2021). Aerosol invigoration of atmospheric convection through increases in humidity. *Science*, *371*(6524), 83–85. https://doi.org/10.1126/science.abc5181

Abbott, T. H., & Cronin, T. W. (2023). Multiple equilibria and soil moisture-precipitation feedbacks in idealized convection-permitting simulations with an open hydrological cycle. *Journal of Advances in Modeling Earth Systems*, *15*(8), e2023MS003719. https://doi.org/10.1029/2023MS003719

Alchapar, N. L., Pezzuto, C. C., Correa, E. N., & Chebel Labaki, L. (2017). The impact of different cooling strategies on urban air temperatures: The cases of Campinas, Brazil and Mendoza, Argentina. *Theoretical and Applied Climatology*, *130*(1–2), 35–50. https://doi.org/10.1007/s00704-016-1851-5

Baidya Roy, S., & Avissar, R. (2002). Impact of land use/land cover change on regional hydrometeorology in Amazonia. *Journal of Geophysical Research*, *107*(D20), LBA4-1–LBA4-12. https://doi.org/10.1029/2000JD000266

Baidya Roy, S., Weaver, C. P., Nolan, D. S., & Avissar, R. (2003). A preferred scale for landscape forced mesoscale circulations? *Journal of Geophysical Research*, *108*(D22). https://doi.org/10.1029/2002JD003097

Brutsaert, W., & Sugita, M. (1992). Application of self-preservation in the diurnal evolution of the surface energy budget to determine daily evaporation. *Journal of Geophysical Research*, *97*(D17), 18377–18382. https://doi.org/10.1029/92JD00255

Chakraborty, T., Newman, A. J., Qian, Y., Hsu, A., & Sheriff, G. (2023). Residential segregation and outdoor urban moist heat stress disparities in the United States. *One Earth*, *6*(6), 738–750. https://doi.org/10.1016/j.oneear.2023.05.016

Chakraborty, T., Venter, Z., Qian, Y., & Lee, X. (2022). Lower urban humidity moderates outdoor heat stress. *AGU Advances*, *3*(5), e2022AV000729. https://doi.org/10.1029/2022AV000729

Charney, J. G., Quirk, W. J., Chow, S.-H., & Kornfield, J. (1977). A comparative study of the effects of albedo change on drought in semi–arid regions. *Journal of the Atmospheric Sciences*, *34*(9), 1366–1385. https://doi.org/10.1175/1520-0469(1977)034<1366:ACSOTE>2.0.CO;2

Cheng, Y., Chan, P. W., Wei, X., Hu, Z., Kuang, Z., & McColl, K. A. (2021). Soil moisture control of precipitation re-evaporation over a heterogeneous land surface. *Journal of the Atmospheric Sciences*, *78*(10), 3369–3383. https://doi.org/10.1175/JAS-D-21-0059.1

Cheng, Y., Hu, Z., & McColl, K. A. (2023). Anomalously darker land surfaces become wetter due to mesoscale circulations. *Geophysical Research Letters*, *50*(17), e2023GL104137. https://doi.org/10.1029/2023GL104137

Cheng, Y., & McColl, K. (2024). Replication Data for: Unexpected warming from land radiative management. https://doi.org/10.7910/DVN/ZEGHDW

Cheng, Y., & McColl, K. A. (2023). Thermally direct mesoscale circulations caused by land surface roughness anomalies. *Geophysical Research Letters*, *50*(16), e2023GL105150. https://doi.org/10.1029/2023GL105150

Cioni, G., & Hohenegger, C. (2017). Effect of soil moisture on diurnal convection and precipitation in large-eddy simulations. *Journal of Hydrometeorology*, *18*(7), 1885–1903. https://doi.org/10.1175/JHM-D-16-0241.1

Davin, E. L., Seneviratne, S. I., Ciais, P., Olioso, A., & Wang, T. (2014). Preferential cooling of hot extremes from cropland albedo management. *Proceedings of the National Academy of Sciences of the United States of America*, *111*(27), 9757–9761. https://doi.org/10.1073/pnas.1317323111

Driedonks, A. (1982). Sensitivity analysis of the equations for a convective mixed layer. *Boundary-Layer Meteorology*, *22*(4), 475–480. https://doi.org/10.1007/BF00124706

ECMWF. (2016). *IFS documentation cy43r1—Part IV: Physical processes*. European Centre for Medium-Range Weather Forecasts. https://doi.org/10.21957/sqvo5yxja

Erell, E., Pearlmutter, D., Boneh, D., & Kutiel, P. B. (2014). Effect of high-albedo materials on pedestrian heat stress in urban street canyons. *Urban Climate*, *10*, 367–386. https://doi.org/10.1016/j.uclim.2013.10.005

Fallmann, J., Emeis, S., & Suppan, P. (2013). Mitigation of urban heat stress–a modelling case study for the area of Stuttgart. *DIE ERDE–Journal of the Geographical Society of Berlin*, *144*(3–4), 202–216. https://doi.org/10.12854/erde-144-15

Garratt, J. (1992). *The atmospheric boundary layer*. Cambridge University Press.

Gentine, P., Entekhabi, D., Chehbouni, A., Boulet, G., & Duchemin, B. (2007). Analysis of evaporative fraction diurnal behaviour. *Agricultural and Forest Meteorology*, *143*(1–2), 13–29. https://doi.org/10.1016/j.agrformet.2006.11.002

Gilabert, J., Ventura, S., Segura, R., Martilli, A., Badia, A., Llasat, C., et al. (2021). Abating heat waves in a coastal Mediterranean city: What can cool roofs and vegetation contribute? *Urban Climate*, *37*, 100863. https://doi.org/10.1016/j.uclim.2021.100863

Held, I. M., Hemler, R. S., & Ramaswamy, V. (1993). Radiative-convective equilibrium with explicit two-dimensional moist convection. *Journal of the Atmospheric Sciences*, *50*(23), 3909–3927. https://doi.org/10.1175/1520-0469(1993)050<3909:RCEWET>2.0.CO;2

Hirsch, A. L., Wilhelm, M., Davin, E. L., Thiery, W., & Seneviratne, S. I. (2017). Can climate-effective land management reduce regional warming? *Journal of Geophysical Research: Atmospheres*, *122*(4), 2269–2288. https://doi.org/10.1002/2016JD026125

Hsu, A., Sheriff, G., Chakraborty, T., & Manya, D. (2021). Disproportionate exposure to urban heat island intensity across major US cities. *Nature Communications*, *12*(1), 2721. https://doi.org/10.1038/s41467-021-22799-5

Irvine, P. J., Ridgwell, A., & Lunt, D. J. (2011). Climatic effects of surface albedo geoengineering. *Journal of Geophysical Research*, *116*(D24). https://doi.org/10.1029/2011JD016281

Jacobs, S. J., Gallant, A. J., Tapper, N. J., & Li, D. (2018). Use of cool roofs and vegetation to mitigate urban heat and improve human thermal stress in Melbourne, Australia. *Journal of Applied Meteorology and Climatology*, *57*(8), 1747–1764. https://doi.org/10.1175/JAMC-D-17-0243.1

Jia, G., Shevliakova, E., Artaxo, P., Zhou, Y., de Noblet, N., Houghton, R., et al. (2019). IPCC SRCCL chapter 2: Land-climate interactions (pp. 133–206).

Khairoutdinov, M. F., & Randall, D. A. (2003). Cloud resolving modeling of the arm summer 1997 IOP: Model formulation, results, uncertainties, and sensitivities. *Journal of the Atmospheric Sciences*, *60*(4), 607–625. https://doi.org/10.1175/1520-0469(2003)060<0607:CRMOTA>2.0.CO;2

Kiehl, J., Hack, J., Bonan, G., Boville, B., Williamson, D., & Rasch, P. (1998). The national center for atmospheric research community climate model: CCM3. *Journal of Climate*, *11*(6), 1131–1149. https://doi.org/10.1175/1520-0442(1998)011<1131:TNCFAR>2.0.CO;2

Koster, R. D., Guo, Z., Yang, R., Dirmeyer, P. A., Mitchell, K., & Puma, M. J. (2009). On the nature of soil moisture in land surface models. *Journal of Climate*, *22*(16), 4322–4335. https://doi.org/10.1175/2009JCLI2832.1

Koster, R. D., & Mahanama, S. P. (2012). Land surface controls on hydroclimatic means and variability. *Journal of Hydrometeorology*, *13*(5), 1604–1620.

Lee, J. M., & Khairoutdinov, M. (2015). A simplified land model (SLM) for use in cloud-resolving models: Formulation and evaluation. *Journal of Advances in Modeling Earth Systems*, *7*(3), 1368–1392. https://doi.org/10.1002/2014MS000419

Lehner, F., & Deser, C. (2023). Origin, importance, and predictive limits of internal climate variability. *Environmental Research: Climate*, *2*(2), 023001. https://doi.org/10.1088/2752-5295/accf30

Li, D., Bou-Zeid, E., & Oppenheimer, M. (2014). The effectiveness of cool and green roofs as urban heat island mitigation strategies. *Environmental Research Letters*, *9*(5), 055002. https://doi.org/10.1088/1748-9326/9/5/055002

Lynn, B. H., Carlson, T. N., Rosenzweig, C., Goldberg, R., Druyan, L., Cox, J., et al. (2009). A modification to the NOAH LSM to simulate heat mitigation strategies in the New York city metropolitan area. *Journal of Applied Meteorology and Climatology*, *48*(2), 199–216. https://doi.org/10.1175/2008JAMC1774.1

Mackey, C. W., Lee, X., & Smith, R. B. (2012). Remotely sensing the cooling effects of city scale efforts to reduce urban heat island. *Building and Environment*, *49*, 348–358. https://doi.org/10.1016/j.buildenv.2011.08.004

Manabe, S., & Strickler, R. F. (1964). Thermal equilibrium of the atmosphere with a convective adjustment. *Journal of the Atmospheric Sciences*, *21*(4), 361–385. https://doi.org/10.1175/1520-0469(1964)021<0361:TEOTAW>2.0.CO;2

Middel, A., Chhetri, N., & Quay, R. (2015). Urban forestry and cool roofs: Assessment of heat mitigation strategies in phoenix residential neighborhoods. *Urban Forestry and Urban Greening*, *14*(1), 178–186. https://doi.org/10.1016/j.ufug.2014.09.010

Miyawaki, O., Shaw, T. A., & Jansen, M. F. (2022). Quantifying energy balance regimes in the modern climate, their link to lapse rate regimes, and their response to warming. *Journal of Climate*, *35*(3), 1045–1061. https://doi.org/10.1175/JCLI-D-21-0440.1

Monin, A., & Obukhov, A. (1954). Basic laws of turbulent mixing in the surface layer of the atmosphere. In *Contributions of the Geophysical Institute of the Slovak Academy of Sciences* (Vol. 151, p. e187).

Patton, E. G., Sullivan, P. P., & Moeng, C.-H. (2005). The influence of idealized heterogeneity on wet and dry planetary boundary layers coupled to the land surface. *Journal of the Atmospheric Sciences*, *62*(7), 2078–2097. https://doi.org/10.1175/JAS3465.1

Physick, W., & Tapper, N. (1990). A numerical study of circulations induced by a dry salt lake. *Monthly Weather Review*, *118*(5), 1029–1042. https://doi.org/10.1175/1520-0493(1990)118<1029:ANSOCI>2.0.CO;2

Porporato, A. (2009). Atmospheric boundary-layer dynamics with constant Bowen ratio. *Boundary-Layer Meteorology*, *132*(2), 227–240. https://doi.org/10.1007/s10546-009-9400-8

Raymond, D. J., & Zeng, X. (2005). Modelling tropical atmospheric convection in the context of the weak temperature gradient approximation. *The Quarterly Journal of the Royal Meteorological Society*, *131*(608), 1301–1320. https://doi.org/10.1256/qj.03.97

Sakaguchi, K., Berg, L. K., Chen, J., Fast, J., Newsom, R., Tai, S.-L., et al. (2022). Determining spatial scales of soil moisture—Cloud coupling pathways using semi-idealized simulations. *Journal of Geophysical Research: Atmospheres*, *127*(2), e2021JD035282. https://doi.org/10.1029/2021JD035282

Seneviratne, S. I., Corti, T., Davin, E. L., Hirschi, M., Jaeger, E. B., Lehner, I., et al. (2010). Investigating soil moisture–climate interactions in a changing climate: A review. *Earth-Science Reviews*, *99*(3–4), 125–161. https://doi.org/10.1016/j.earscirev.2010.02.004

Seneviratne, S. I., Phipps, S. J., Pitman, A. J., Hirsch, A. L., Davin, E. L., Donat, M. G., et al. (2018). Land radiative management as contributor to regional-scale climate adaptation and mitigation. *Nature Geoscience*, *11*(2), 88–96. https://doi.org/10.1038/s41561-017-0057-5

Sharma, A., Conry, P., Fernando, H., Hamlet, A. F., Hellmann, J., & Chen, F. (2016). Green and cool roofs to mitigate urban heat island effects in the Chicago Metropolitan area: Evaluation with a regional climate model. *Environmental Research Letters*, *11*(6), 064004. https://doi.org/10.1088/1748-9326/11/6/064004

Sobel, A. H., Nilsson, J., & Polvani, L. M. (2001). The weak temperature gradient approximation and balanced tropical moisture waves. *Journal of the Atmospheric Sciences*, *58*(23), 3650–3665. https://doi.org/10.1175/1520-0469(2001)058<3650:TWTGAA>2.0.CO;2

Stahl, M. O., & McColl, K. A. (2022). The seasonal cycle of surface soil moisture. *Journal of Climate*, *35*(15), 4997–5012. https://doi.org/10.1175/JCLI-D-21-0780.1

Synnefa, A., Dandou, A., Santamouris, M., Tombrou, M., & Soulakellis, N. (2008). On the use of cool materials as a heat island mitigation strategy. *Journal of Applied Meteorology and Climatology*, *47*(11), 2846–2856. https://doi.org/10.1175/2008JAMC1830.1

Taleghani, M., Sailor, D., & Ban-Weiss, G. A. (2016). Micrometeorological simulations to predict the impacts of heat mitigation strategies on pedestrian thermal comfort in a Los Angeles neighborhood. *Environmental Research Letters*, *11*(2), 024003. https://doi.org/10.1088/1748-9326/11/2/024003

Taylor, C. M., Klein, C., Parker, D. J., Gerard, F., Semeena, V. S., Barton, E. J., & Harris, B. L. (2022). "late-stage" deforestation enhances storm trends in coastal west Africa. *Proceedings of the National Academy of Sciences of the United States of America*, *119*(2). https://doi.org/10.1073/pnas.2109285119

Tennekes, H. (1973). A model for the dynamics of the inversion above a convective boundary layer. *Journal of the Atmospheric Sciences*, *30*(4), 558–567. https://doi.org/10.1175/1520-0469(1973)030<0558:AMFTDO>2.0.CO;2

Tian, J., Zhang, Y., Klein, S. A., Öktem, R., & Wang, L. (2022). How does land cover and its heterogeneity length scales affect the formation of summertime shallow cumulus clouds in observations from the us southern great plains? *Geophysical Research Letters*, *49*(7), e2021GL097070. https://doi.org/10.1029/2021GL097070

Vahmani, P., Sun, F., Hall, A., & Ban-Weiss, G. (2016). Investigating the climate impacts of urbanization and the potential for cool roofs to counter future climate change in southern California. *Environmental Research Letters*, *11*(12), 124027. https://doi.org/10.1088/1748-9326/11/12/124027

Wang, J., Bras, R. L., & Eltahir, E. A. (2000). The impact of observed deforestation on the mesoscale distribution of rainfall and clouds in Amazonia. *Journal of Hydrometeorology*, *1*(3), 267–286. https://doi.org/10.1175/1525-7541(2000)001<0267:TIOODO>2.0.CO;2

Wilhelm, M., Davin, E. L., & Seneviratne, S. I. (2015). Climate engineering of vegetated land for hot extremes mitigation: An Earth system model sensitivity study. *Journal of Geophysical Research: Atmospheres*, *120*(7), 2612–2623. https://doi.org/10.1002/2014JD022293

Unexpected warming from land radiative management

Yu Cheng[1], **Kaighin A. McColl**[1,2]

[1]Department of Earth and Planetary Sciences, Harvard University, Cambridge, Massachusetts, USA
[2]School of Engineering and Applied Sciences, Harvard University, Cambridge, Massachusetts, USA

Contents of this file

1 Materials and Methods

1.1 Mesoscale convection-permitting simulations

We simulate the atmospheric response to a high albedo anomaly in a low albedo background using convection-permitting simulations over an idealized land surface (Fig. S1). The System for Atmospheric Modeling (SAM (Khairoutdinov & Randall, 2003); version 6.11.8) is used as the convection-permitting model. The land surface model introduced in Lee and Khairoutdinov (2015) is applied here. The land cover type is bare soil and is spatially homogeneous. The National Center for Atmospheric Research (NCAR) Community Climate Model (CCM3) radiative transfer scheme is used to compute longwave and shortwave radiation (Kiehl et al., 1998). The prognostic turbulent kinetic energy budget model with a 1.5-order closure scheme (Khairoutdinov & Randall, 2003) is used as the subgrid-scale (SGS) turbulence scheme. The single-moment SAM1MOM scheme is used to predict the mixing ratios of hydrometeor species (Khairoutdinov & Randall, 2003). The simulations start on January 1 and are run for 1000 days with a diurnal cycle for all RCE simulations listed in Table S1. The lengths of simulation for A_WTG and B_WTG are 796 days and 1033 days, respectively. No seasonal cycle is prescribed.

Two types of model domain are prescribed to examine the effects of LRM at different spatial scales (Fig. S1). The domain is periodic in both x and y directions. The vertical resolution is 30 m near the surface and 200 m near the top of the domain. In Domain A, the total size of the domain is 400 km $\times$ 50 km $\times$ 22 km, with a horizontal resolution of 1 km. A high-albedo rectangle is placed at the center of the domain, corresponding to the LRM region (Fig. S1a). In Domain B, the total size of the domain is 25 km $\times$ 25 km $\times$ 22 km, with a horizontal resolution of 250 m. A high-albedo square is placed at the center of the domain, corresponding to the LRM region (Fig. S1b).

In our simulations, the large-scale atmospheric dynamics are simplified using two different approximations: radiative convective equilibrium (RCE (Manabe & Strickler, 1964; Held et al., 1993)) and the weak temperature gradient approximation (WTG (Sobel et al., 2001)). RCE refers to a statistically stationary state of balance between radiative cooling and convective heating. While only strictly applicable to the global mean, RCE is often used as a reasonable approximation of tropical climate. In addition, recent work has shown that the presence of land extends its applicability as a reasonable approximation well beyond the tropics, particularly in summer (Miyawaki et al., 2022). RCE configurations have been applied to convection-permitting simulations of similar problems (Cioni & Hohenegger, 2018; Cheng et al., 2021).

Corresponding author: Kaighin A. McColl, kmccoll@seas.harvard.edu

The WTG approximation (Sobel et al., 2001) has been applied extensively in previous studies of tropical climate over a limited domain (Raymond & Zeng, 2005; Abbott & Cronin, 2023; Cheng & McColl, 2023) to model the interaction between convection and large-scale forcing. It approximates horizontal temperature gradients in the free troposphere as negligible, as observed in the tropics. It primarily differs from RCE in that mean air ascent or descent is permitted, which is an arguably closer approximation of the tropical atmosphere over our limited simulation domain. The cost of this greater realism is dependence on a specified reference temperature profile. We use the same reference temperature profile as in Abbott and Cronin (2021).

Solar insolation is varied to represent a broad range of climates. For Domain A, a range of simulations are performed with solar insolation varying between that centered at latitude 15 °N and 20 °N (Table S2). Because our simulations are of idealized land regions, the resulting climates span a much wider range than the corresponding climates of Earth at these latitudes. For example, the resulting simulations' domain-averaged near-surface air temperatures vary between 11 °C and 41 °C during the day (Fig. S2). For Domain B, one simulation is performed with solar insolation corresponding to that at 8°N.

We focus on the near-surface air temperature (T_a) rather than surface temperature because it is most relevant to human health (Chakraborty et al., 2022). The standard measurement height for this quantity is 2 m above the surface. Since T_a is not an output provided by the cloud-permitting simulations, we estimate it by interpolating between land surface temperature and the simulated air temperature nearest to the surface (15 m above the surface in our simulations). The interpolation follows the standard operational implementation of the ECMWF model (ECMWF, 2016), and invokes Monin-Obukhov similarity theory (Monin & Obukhov, 1954).

Since the mean temperatures of our simulations vary considerably, we focus on temperature anomalies to more clearly compare the simulations. Specifically, we estimate the difference between the time-averaged temperature, and the time- and space-averaged temperature far from the LRM region (Fig. S3). We define a region as being "far" from the LRM region if it is greater than 90 km from it, although our results are not particularly sensitive to this choice of threshold. Positive (negative) anomalies imply that LRM causes warming (cooling), assuming that LRM does not substantially impact temperatures far from the LRM region.

The observed warming outside the LRM region is still observed when the following changes are made to our simulations: (1) adding a prescribed mean wind (A_RCE_wind, Fig. S4); (2) using the WTG approximation (A_WTG, Fig. S5) instead of RCE; (3) using a smaller domain size and LRM region, and a finer resolution (B_WTG, Fig. S6).

To test the assumption that LRM does not substantially impact temperatures far from the LRM region, we run one additional control simulation (A_RCE_ctl, Table S1), in which there is no LRM region but the domain-averaged surface albedo is identical to that in the relevant LRM simulation (A_RCE, Table S1). The domain-averaged temperature in the control simulation is statistically indistinguishable from the temperature far from the LRM region in A_RCE, confirming that this approximation is reasonable. We obtain qualitatively similar results estimating anomalies using the control simulation as the reference temperature (Figs. S7 and S8).

Finally, a simulation is performed that is identical to A_RCE at a latitude of 19°, except soil moisture is held fixed at the domain-averaged value (A_RCE_fixsoil, Fig. S9). Some warming still occurs outside the LRM boundary but its magnitude is significantly reduced, suggesting that our explanation in terms of soil moisture appears to be the dominant reason for the anomalous warming.

1.2 Conceptual model

This section describes the conceptual model used to understand results from the mesoscale simulations.

1.2.1 Logistic models for precipitation and net radiation

Near the boundary between the high albedo LRM region and low albedo background, we assume that the $x-$direction profiles of both precipitation (P) and net radiation at the land surface (R_n) can be represented by logistic functions (Figs. 3a and b):

$$P(x) = P_H + \frac{P_0 - P_H}{1 + \exp(-(|x| - L)/L_P)}, \tag{S1}$$

$$R_n(x) = R_{n_H} + \frac{R_{n_0} - R_{n_H}}{1 + \exp(-(|x| - L)/L_{R_n})}, \tag{S2}$$

where terms with an "H" subscript correspond to values in the LRM region, terms with a "0" subscript correspond to values far from the LRM region, L is the half-width of the LRM region (with the center of the LRM region at $x = 0$, and the entire LRM region located in the range $|x| < L$), and L_P and L_{R_n} are length scales over which P and R_n transition from their lower values in the LRM region to higher values outside the LRM region, respectively. Since the atmosphere is turbulent and strongly mixed compared to the land surface, we expect $L_P \gg L_{R_n}$. Fitting these functions to profiles of precipitation and net radiation from our simulations confirms this expectation. Estimated values of L_P vary between 0.83 km and 1.48 km in experiments A_RCE (Table S1). Estimated values of L_{R_n} are all much smaller than the grid resolution of the simulations, implying that it is indistinguishable from zero in our simulations.

1.2.2 Soil saturation and surface fluxes

We use the models of precipitation and net radiation provided in the previous section to estimate profiles of soil saturation and surface sensible heat fluxes. Soil saturation is defined as

$$s = \frac{\phi - \phi_{\mathrm{w}}}{\phi_{\mathrm{fc}} - \phi_{\mathrm{w}}}, \tag{S3}$$

where ϕ is the ratio of the volume of water to the unit volume of soil ($\mathrm{m}^3\ \mathrm{m}^{-3}$), ϕ_{w} ($\mathrm{m}^3\ \mathrm{m}^{-3}$) is the wilting point soil moisture, and ϕ_{fc} ($\mathrm{m}^3\ \mathrm{m}^{-3}$) is the field capacity (an approximate upper bound for soil water storage). Soil saturation is estimated using a recent theory (Stahl & McColl, 2022) that requires precipitation and net radiation as inputs,

$$s = \frac{\rho_w \lambda P}{\alpha R_n + \rho_w \lambda P}, \tag{S4}$$

where ρ_w is the density of water ($\mathrm{kg\ m}^{-3}$), λ is the latent heat of vaporization ($\mathrm{J\ kg}^{-1}$), precipitation has units of $\mathrm{m\ s}^{-1}$, net radiation has units of $\mathrm{W\ m}^{-2}$, and α is a constant parameter set to 0.8 based on prior studies (Milly & Dunne, 2016). Our results are not qualitatively sensitive to the exact choice of this parameter. This theory, which is derived from an idealized land surface water balance, was originally proposed for explaining variability in the seasonal cycle of soil moisture. However, Scheff and Frierson (2015) showed that a similar model was successful in explaining variability in the evaporative fraction in climate models; and, the evaporative fraction is a proxy for soil moisture in water-limited regions (Koster & Mahanama, 2012; Seneviratne et al., 2010). The theory's predictions correlate well with simulated soil saturation (Fig. S10). The absolute values of soil saturation predicted by the theory exhibit some bias, as is typical of most soil moisture models (Koster et al., 2009). Equation S4 qualitatively reproduces our simulated soil moisture profiles, including the distinctive discontinuity at the boundary of the LRM region (Figs. 2c and 3c).

Next, we link soil saturation to the surface sensible heat flux. In the derivation of the simple soil moisture model, we assume that the evaporative fraction (the ratio of surface latent heat flux to the sum of surface latent and sensible heat fluxes) is linearly related to the soil saturation:

$$\frac{\lambda E}{\lambda E + H} = \epsilon s + \eta, \tag{S5}$$

where H is the surface sensible heat flux and ϵ and η are parameters. This is a common approximation for water-limited regions (Koster & Mahanama, 2012; Seneviratne et al., 2010). Our numerical simulations suggest that ϵ and η are constant in individual experiments but vary between experiments at different latitudes (Figs. S11 and S12). The coefficient of determination (R^2) for the linear fit between $\frac{\lambda E}{\lambda E+H}$ and s is more than 0.97 for each numerical simulation (Fig. S12).

Rearranging this expression yields

$$H = (1 - \epsilon s - \eta) R_n. \tag{S6}$$

where we have used the surface energy balance ($R_n - G = H + \lambda E$) and assumed ground heat flux is negligible. The sensible heat flux can also be written as a function of Bowen ratio,

$$H = R_n \frac{B}{1 + B}, \tag{S7}$$

where the Bowen ratio B is the ratio of sensible and latent heat fluxes.

1.2.3 Bulk mixed layer model

To relate the surface sensible heat flux to near-surface air temperature, we use a simplified bulk mixed layer model of the atmospheric boundary layer (ABL). The model follows a standard formulation (Tennekes, 1973; Garratt, 1992; Porporato, 2009), and results in the following equations,

$$\frac{dh}{dt} = \frac{(1 + 2\beta) H}{\rho c_p \gamma_\theta h}, \tag{S8}$$

and

$$\rho c_p h \frac{d\theta}{dt} = H + \rho c_p (\theta_f - \theta) \frac{dh}{dt}, \tag{S9}$$

where h is the height of the ABL, θ is the potential temperature in the mixed layer, t is time, γ_θ is the potential temperature lapse rate of the free atmosphere, β is an entrainment parameter, ρ is the density of the air, and c_p is the specific heat of air at constant pressure. θ_f is the potential temperature of the free atmosphere at ABL height given by the following linear profile (Tennekes, 1973; Porporato, 2009)

$$\theta_f = \theta_{f_0} + \gamma_\theta h, \tag{S10}$$

where θ_{f_0} would be the potential temperature at the surface if there was no mixed layer and the free-tropospheric temperature profile extended down to the surface. This quantity can be interpreted as approximately equivalent to the near-surface temperature at sunrise, if we neglect the dissipation of the nocturnal residual layer (the 'morning transition'; this approximation is discussed further in Porporato (2009)). We assume there is no significant spatial structure to θ_{f_0}, which implies that near-surface temperatures reset to a common value everywhere in the domain overnight. As shown in previous studies (Driedonks, 1982; Porporato, 2009), combining Equations S8, S9 and S10, a linear relationship between potential temperature in the mixed layer and ABL height is obtained,

$$\theta - \theta_{f_0} = \gamma_\theta \frac{1 + \beta}{1 + 2\beta} h. \tag{S11}$$

To relate this to the surface sensible heat flux, we use two additional simplifications, which were both used previously in Porporato (2009). First, the Bowen ratio (the ratio of sensible heat flux to latent heat flux) is assumed approximately constant during the day, as observed in field experiments (Brutsaert & Sugita, 1992). Since the Bowen ratio is a one-to-one function of the evaporative fraction, this implies the evaporative fraction is also approximately constant during the day (Gentine et al., 2007). Second, the diurnal cycle of net radiation is assumed to follow a parabolic relation in time, peaking at noon,

$$R_n(t) = R_n^{\max}\left(1 - \left(\frac{t}{t_0} - 1\right)^2\right), \tag{S12}$$

where $R_n^{\max}$ is peak daily surface net radiation, t_0 is half of the daytime length (i.e., 6 hours), and $0 < t < 2t_0$. This implies that the daytime-averaged net radiation is

$$\langle R_n \rangle = \frac{1}{2t_0}\int_0^{2t_0} R_n(t)dt = \frac{1}{2t_0}\int_0^{2t_0} R_n^{\max}(1 - (t/t_0 - 1)^2)dt = \frac{2}{3}R_n^{\max}. \tag{S13}$$

Combining Equations S7, S8, S12, and S13 and solving the resulting differential equation yields

$$h = \left(\frac{(1+2\beta)}{\rho c_p \gamma_\theta}\langle R_n \rangle \frac{B}{1+B}\frac{(3t_0 - t)t^2}{t_0^2}\right)^{1/2}. \tag{S14}$$

Equation S14 is equivalent to Equation 37 in Porporato (2009). Note that there is a typographical error in Equation 37 of Porporato (2009); it is missing a factor of $Q_m^{1/2}$ in their notation (Porporato, pers. comm.).

Then, combining Equations S6, S7, S11, and S14 results in the relation

$$T_a(t) = \theta_{f_0} + \gamma_\theta \frac{1+\beta}{1+2\beta}\left(\frac{2}{3}\frac{(1+2\beta)}{\rho c_p \gamma_\theta}\frac{(3t_0 - t)t^2}{t_0^2}(1 - \epsilon\langle s \rangle - \eta)R_n^{\max}\right)^{1/2}, \tag{S15}$$

where T_a is near-surface air temperature and is equivalent to potential temperature (θ) in the mixed layer. As the Bowen ratio is assumed constant during the daytime, soil saturation s is assumed to be independent of t and is represented by the daytime average $\langle s \rangle$, where $\langle\rangle$ denotes averaging in the daytime. The daytime-averaged near-surface air temperature is

$$\begin{aligned}
\langle T_a \rangle &= \frac{1}{2t_0}\int_0^{2t_0} T_a(t)dt \\
&= \theta_{f_0} + \frac{\gamma_\theta}{2t_0}\frac{1+\beta}{1+2\beta}\left(\frac{2}{3}\frac{(1+2\beta)}{\rho c_p \gamma_\theta}(1 - \epsilon\langle s \rangle - \eta)R_n^{\max}\right)^{1/2}\int_0^{2t_0}\left(\frac{(3t_0 - t)t^2}{t_0^2}\right)^{1/2}dt \\
&= \theta_{f_0} + \frac{\gamma_\theta}{2t_0}\frac{1+\beta}{1+2\beta}\left(\frac{2}{3}\frac{(1+2\beta)}{\rho c_p \gamma_\theta}(1 - \epsilon\langle s \rangle - \eta)R_n^{\max}\right)^{1/2}\left(\frac{4}{5}t_0^{3/2}(3\sqrt{3} - 2)\right) \\
&= \theta_{f_0} + \frac{1}{2}(1+\beta)\left(\frac{2}{3}\frac{\gamma_\theta t_0}{\rho c_p(1+2\beta)}(1 - \epsilon\langle s \rangle - \eta)R_n^{\max}\right)^{1/2}\left(\frac{4}{5}(3\sqrt{3} - 2)\right).
\end{aligned}$$

Alternatively, this can be written as

$$\begin{aligned}
\langle T_a \rangle - \theta_{f_0} &= \frac{1}{2}(1+\beta)\left(\frac{4}{5}(3\sqrt{3} - 2)\right)\left(\frac{\gamma_\theta t_0}{\rho c_p(1+2\beta)}\right)^{1/2}((1 - \epsilon\langle s \rangle - \eta)\langle R_n \rangle)^{1/2} \\
&\propto \sqrt{(1 - \epsilon\langle s \rangle - \eta)\langle R_n \rangle}.
\end{aligned} \tag{S16}$$

In summary, the conceptual model predicts that $\langle T_a \rangle$ is linearly related to $\sqrt{(1 - \epsilon\langle s \rangle - \eta)\langle R_n \rangle}$, with s given by Equation S4.

1.2.4 Model validation

The conceptual model's predictions fit our numerical simulations reasonably well. Fig. S13 shows the relation between $\langle T_a \rangle$ and $\sqrt{(1 - \epsilon\langle s \rangle - \eta)\langle R_n \rangle}$ in our simulations. The correlations are quite acceptable, and the slope is broadly consistent with back-of-the-envelope calculations. Assuming standard values for parameters and thermodynamic constants ($\beta = 0.2$, $\rho = 1.29$ kg m^{-3}, $c_p = 1005$ J kg^{-1} K^{-1}) and a free tropospheric lapse rate of $\gamma_\theta = 8 \times 10^{-3}$ K m^{-1} results in a predicted slope of approximately 0.5 (Equation S16). In comparison, the slope in our numerical simulations varies between 0.59 to 0.80 (Fig. S13). Mismatch between the conceptual model and the numerical simulations are possibly attributable to several sources. These include simplifications made in the bulk mixed layer model, which neglects advection and thus mesoscale circulations, and which parameterizes entrainment at the top of the mixed layer. They also include our neglect of ground heat flux, which is typically small on long timescales but may be non-trivial during the daytime.

Table S1. List of experiments performed in this study. The center of the simulated domain ranges from 15°N to 20°N for the experiment A_RCE. τ denotes simulation length and Δx denotes horizontal resolution. "High albedo α_H" and "Low albedo α_L" indicate surface albedos used in the high-albedo LRM region and the surrounding background, respectively. "Domain" indicates domain geometry used (Fig. S1). "Large scale forcing?" indicates which approximation was used for atmospheric dynamics: radiative-convective equilibrium (RCE) or the weak temperature gradient approximation (WTG). "Fixed soil moisture?" indicates simulations for which soil moisture was held fixed ('Y') or allowed to interactively vary ('N'). "Mean wind?" indicates simulations for which a mean wind of $U = 10$ m s^{-1} was prescribed ('Y') or not prescribed ('N').

Numerical experiments	Latitudes (°N)	τ (days)	High albedo α_H	Low albedo α_L	Domain	Large scale forcing	Fixed s?	Mean wind?	Δx (m)
A_RCE	15, 16 17, 18 19, 20	1000	0.1425	0.0356	A	RCE	N	N	1000
A_RCE_fixsoil	19	1000	0.1425	0.0356	A	RCE	Y	N	1000
A_RCE_wind	19	1000	0.1425	0.0356	A	RCE	N	Y	1000
A_RCE_ctl	19	1000	0.0412	0.0412	A	RCE	N	N	1000
A_WTG	8	796	0.1425	0.0356	A	WTG	N	N	1000
B_WTG	8	1033	0.1425	0.0356	B	WTG	N	N	250

Table S2. The effective latitude of the simulated domain, top-of-atmosphere insolation, and daytime averaged near-surface air temperature $\overline{\langle T_a \rangle}$ across experiments A_RCE. Here $\langle\rangle$ denotes long-term temporal averaging, and $\overline{\ }$ denotes spatial averaging along the x axis.

Latitudes (°N)	Top-of-atmosphere insolation (W m^{-2})	$\overline{\langle T_a \rangle}$ (°C)
15	546	41
16	535	35
17	524	32
18	514	29
19	452	14
20	438	11

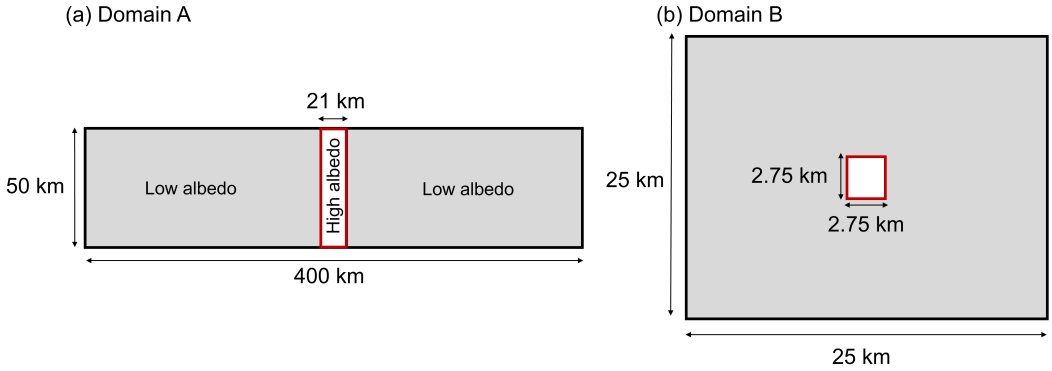

Figure S1. Schematic of simulated domains. In Domain A, the size of the domain is 400 km × 50 km, and the width of the high-albedo rectangle at the center of the domain is 21 km. In Domain B, the size of the domain is 25 km × 25 km, and the length of the side of the high-albedo square at the center of the domain is 2.75 km. Note that the two schematics are not to scale.

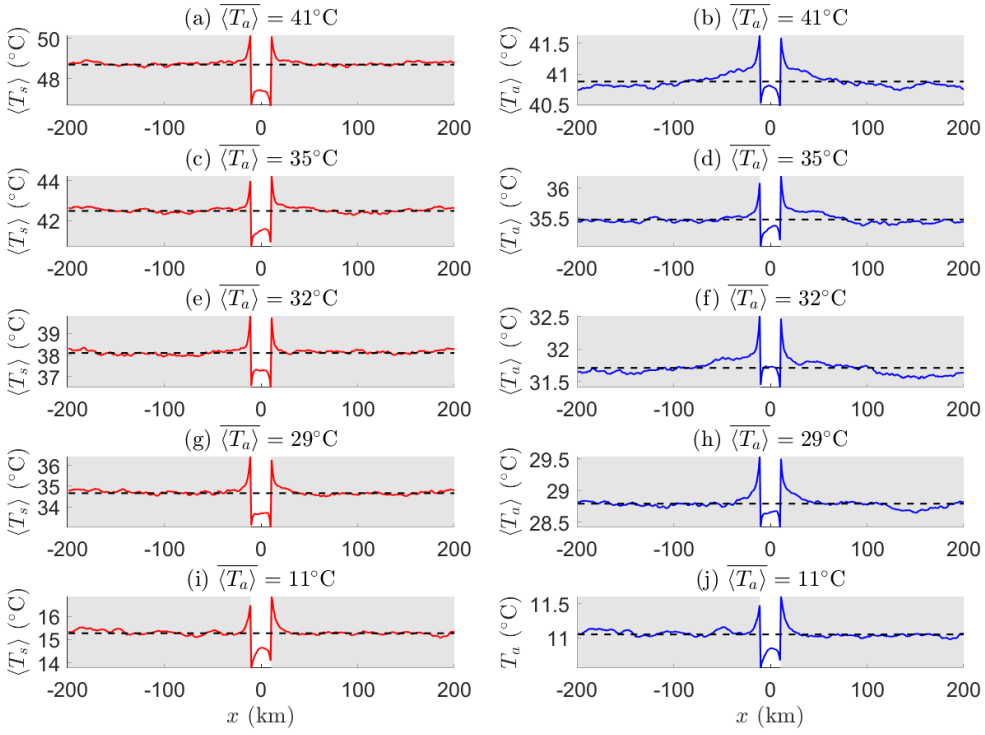

Figure S2. Same as Figure 1b, except showing absolute values of surface temperature (left column) and near-surface air temperature (right column).

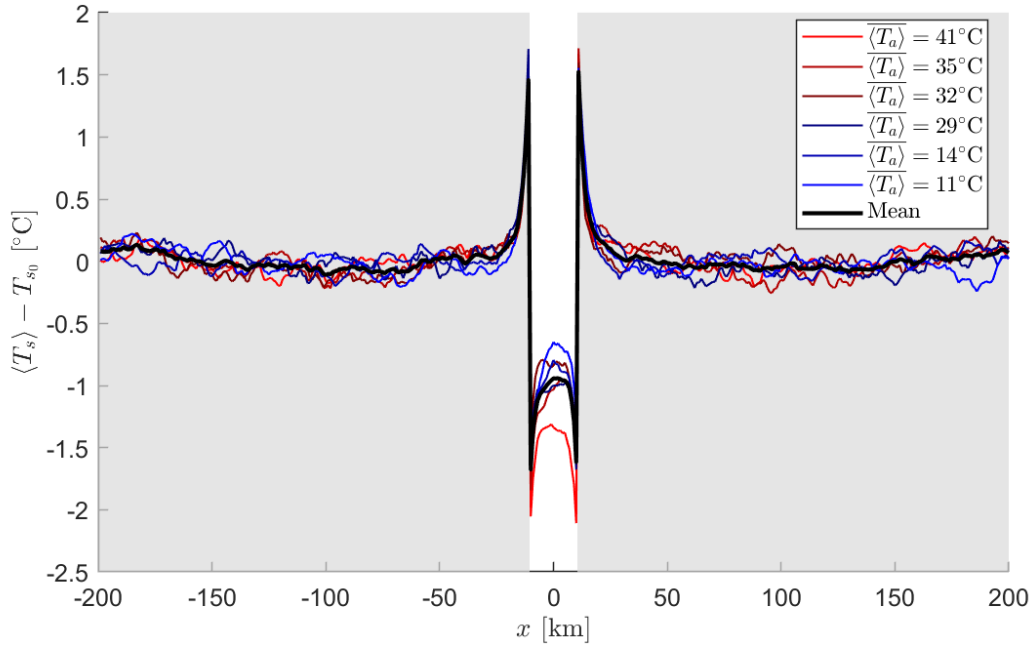

Figure S3. Same as Figure 1b, except for land surface temperature (T_s) rather than near-surface air temperature.

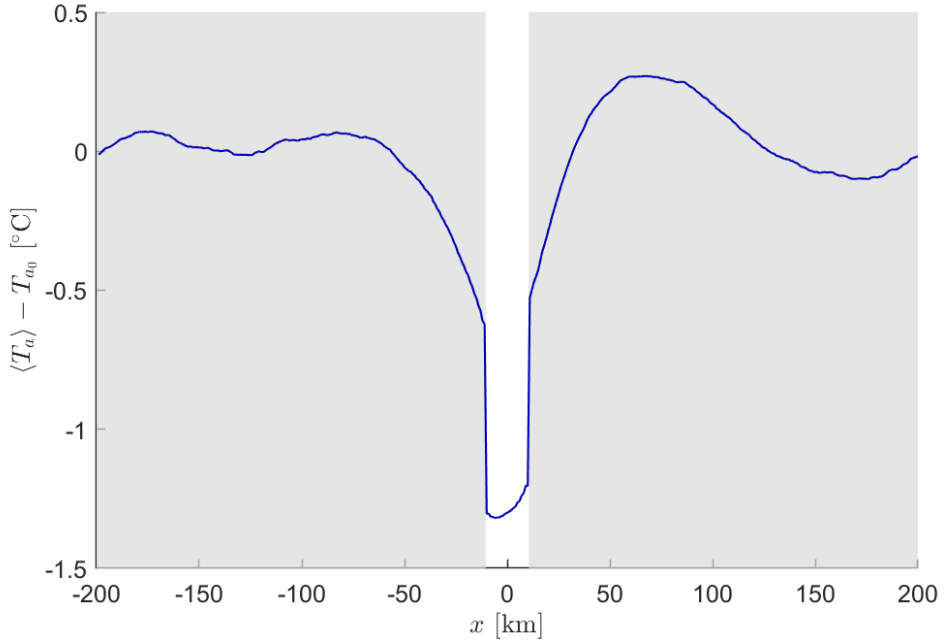

Figure S4. Same as Fig. 1b but for the experiment A_RCE_wind prescribed a mean horizontal wind of 10 m s^{-1} above 400 m (Table S1). This experiment was performed at only one latitude, so only one line is shown in this figure.

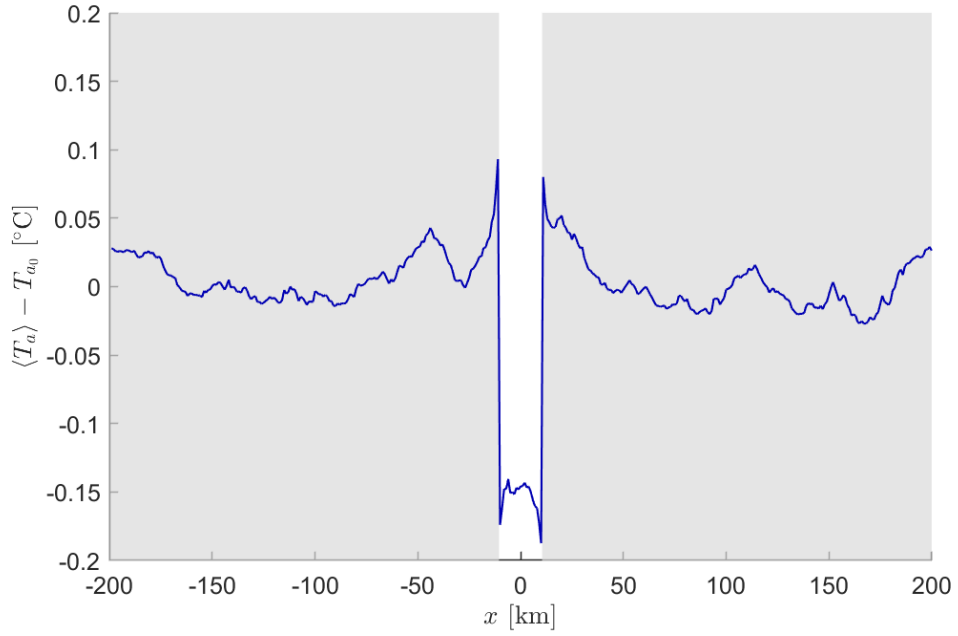

Figure S5. Same as Fig. 1b but for the simulation A_WTG (Table S1). This experiment was performed at only one latitude, so only one line is shown in this figure.

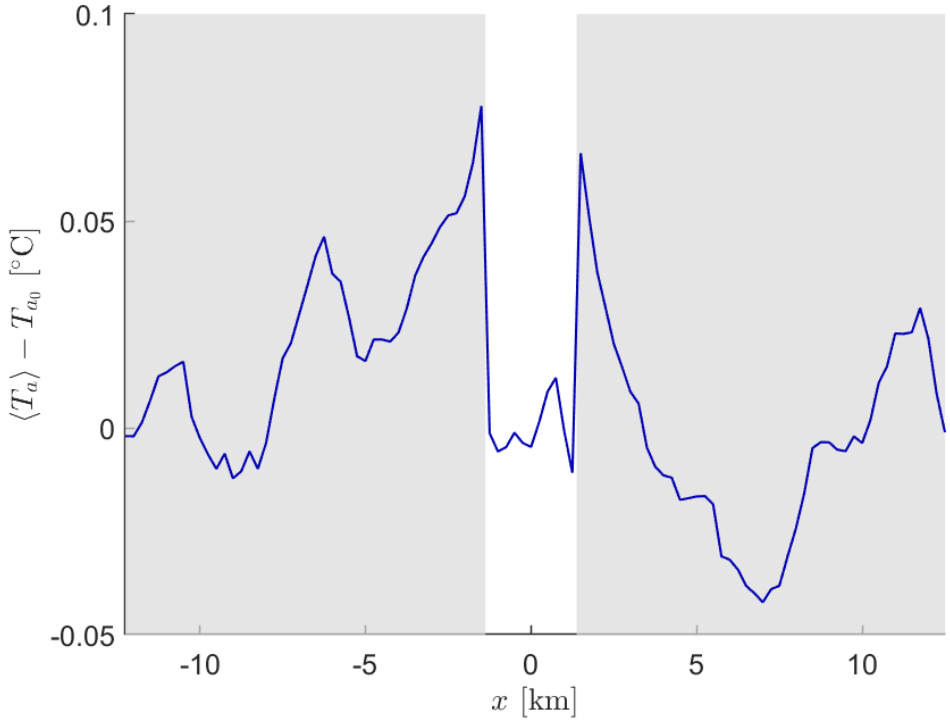

Figure S6. Same as Fig. 1b but for the simulation B_WTG (Table S1). This experiment was performed at only one latitude, so only one line is shown in this figure.

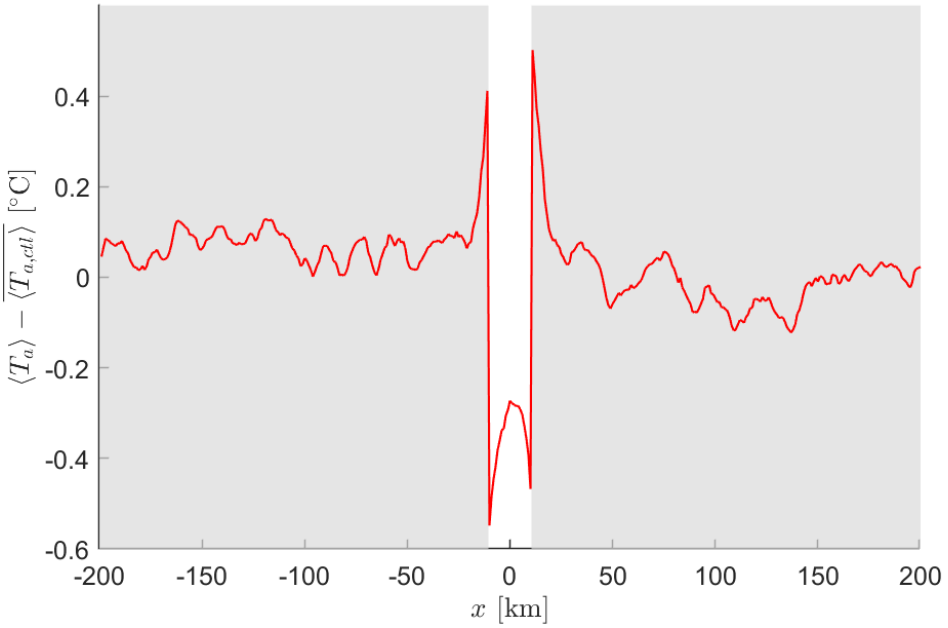

Figure S7. Same as Figure 1b, except using anomalies calculated with respect to the domain-averaged near-surface air temperature in the control simulation A_RCE_ctl (Table S1). A control simulation was performed for only one simulation shown in Figure 1b (A_RCE, $\overline{\langle T_a \rangle} = 14°C$), so only one line is shown in this figure.

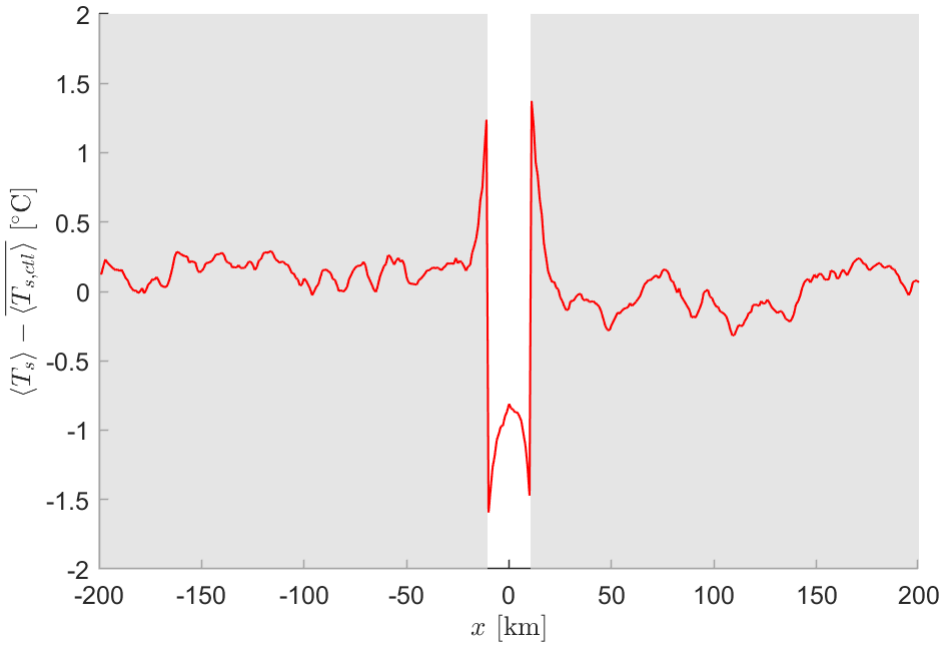

Figure S8. Same as Fig. S7 but for land surface temperature T_s.

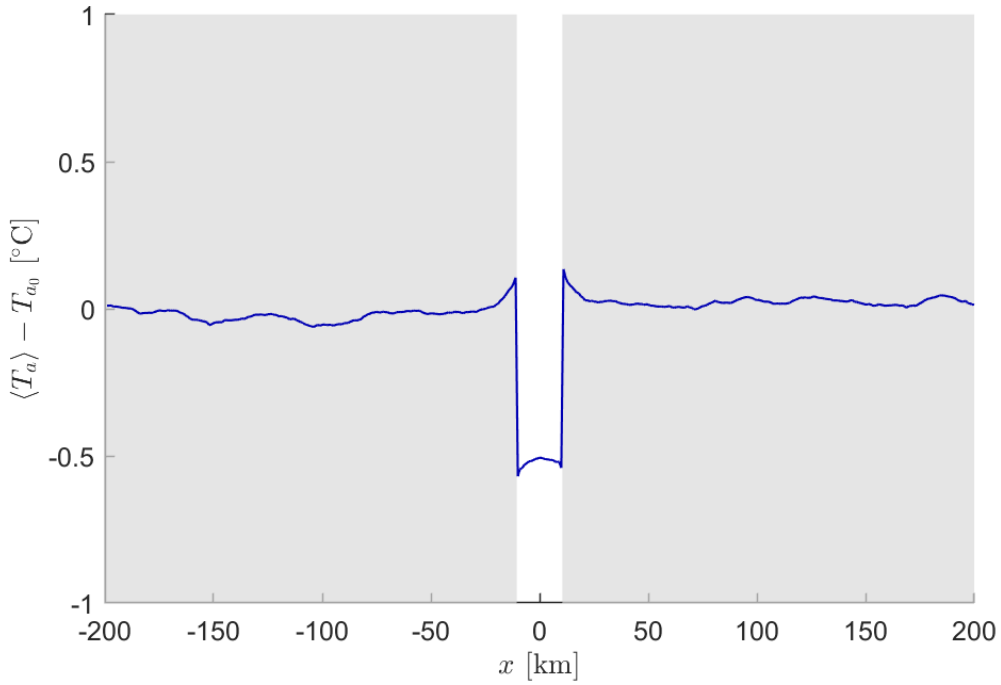

Figure S9. Same as Fig. 1b but for the experiment A_RCE_fixsoil prescribed with fixed soil moisture (Table S1). This experiment was performed at only one latitude, so only one line is shown in this figure.

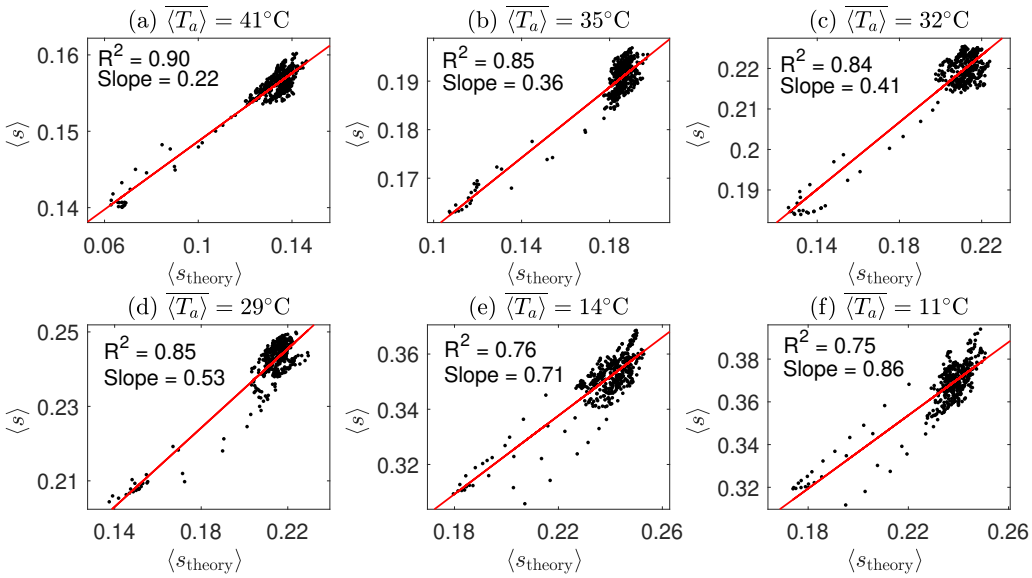

Figure S10. Soil saturation $\langle s \rangle$ from experiments A_RCE at different latitudes and $\langle s_{\text{theory}} \rangle$ computed using Equation S4. A linear regression line is shown (red line), as well as the coefficient of determination R^2 and the slope of the linear regression.

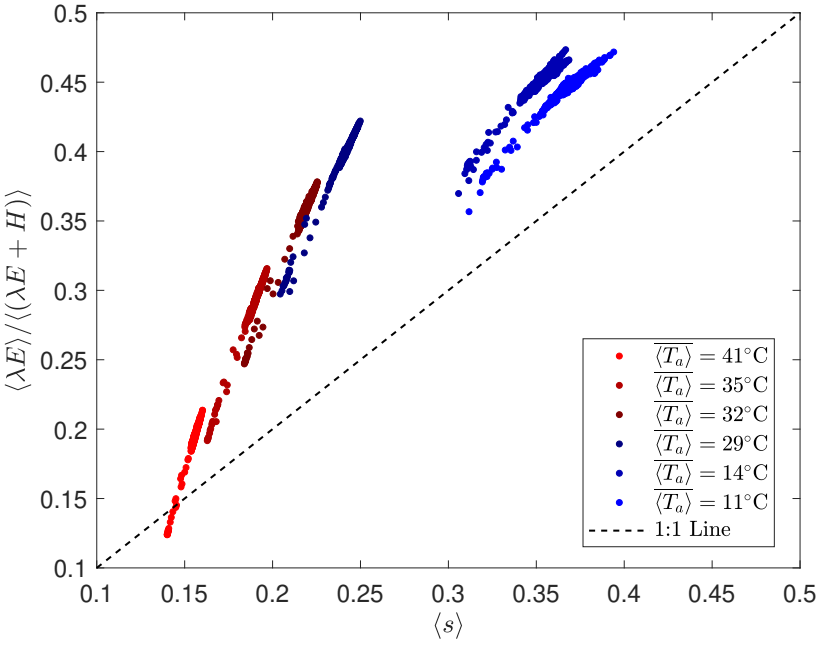

Figure S11. Evaporative fraction $\frac{\langle \lambda E \rangle}{\langle \lambda E + H \rangle}$ and soil saturation $\langle s \rangle$ from experiments A_RCE at different latitudes.

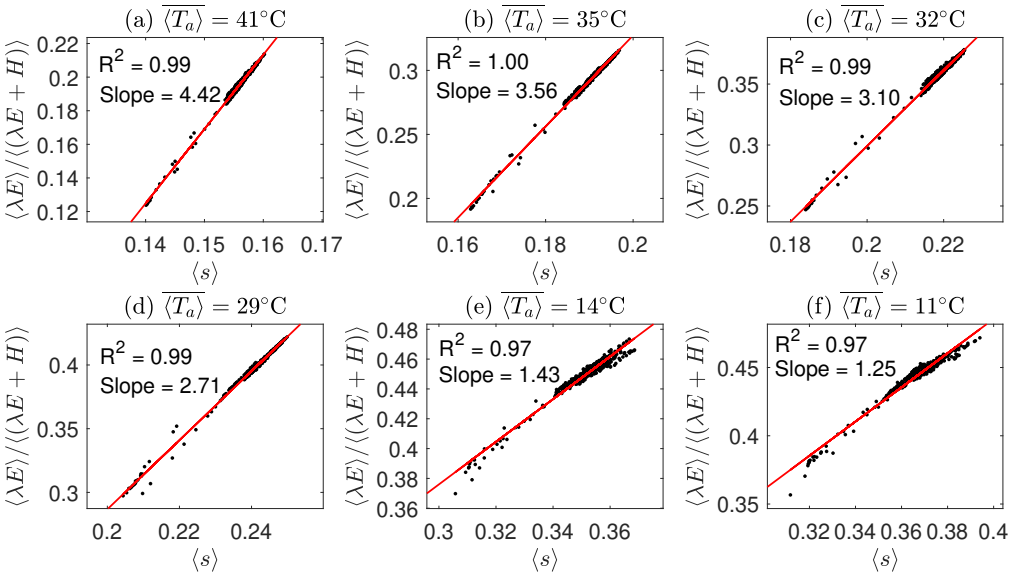

Figure S12. The evaporative fraction $\frac{\langle \lambda E \rangle}{\langle \lambda E + H \rangle}$ and soil saturation $\langle s \rangle$ from experiments A_RCE at different latitudes. A linear regression line is shown (red line), as well as the coefficient of determination R^2 and the slope of the linear regression.

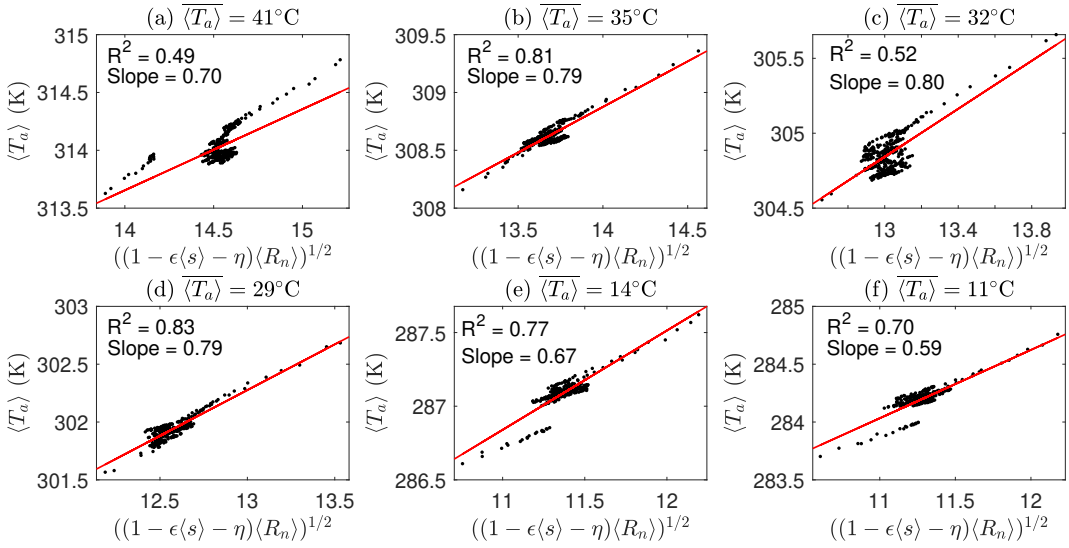

Figure S13. $\langle T_a \rangle$ and $\sqrt{(1-\epsilon\langle s\rangle-\eta)\langle R_n\rangle}$ from experiments A_RCE at different latitudes. A linear regression line is shown (red line), as well as the coefficient of determination R^2 and the slope of the linear regression.

References

Abbott, T. H., & Cronin, T. W. (2021). Aerosol invigoration of atmospheric convection through increases in humidity. *Science*, *371*(6524), 83–85. https://doi.org/10.1126/science.abc5181.

Abbott, T. H., & Cronin, T. W. (2023). Multiple equilibria and soil moisture-precipitation feedbacks in idealized convection-permitting simulations with an open hydrological cycle. *J. Adv. Model. Earth Syst.*, *15*(8), e2023MS003719. https://doi.org/10.1029/2023MS003719.

Brutsaert, W., & Sugita, M. (1992). Application of self-preservation in the diurnal evolution of the surface energy budget to determine daily evaporation. *J. Geophys. Res.-Atmos.*, *97*(D17), 18377–18382. https://doi.org/10.1029/92JD00255.

Chakraborty, T., Venter, Z., Qian, Y., & Lee, X. (2022). Lower urban humidity moderates outdoor heat stress. *AGU adv.*, *3*(5), e2022AV000729. https://doi.org/10.1029/2022AV000729.

Cheng, Y., Chan, P. W., Wei, X., Hu, Z., Kuang, Z., & McColl, K. A. (2021). Soil moisture control of precipitation re-evaporation over a heterogeneous land surface. *J. Atmos. Sci.*, *78*(10), 3369–3383. https://doi.org/10.1175/JAS-D-21-0059.1.

Cheng, Y., & McColl, K. A. (2023). Thermally direct mesoscale circulations caused by land surface roughness anomalies. *Geophys. Res. Lett.*, *50*(16), e2023GL105150. https://doi.org/10.1029/2023GL105150.

Cioni, G., & Hohenegger, C. (2018). A simplified model of precipitation enhancement over a heterogeneous surface. *Hydrol. Earth Syst. Sci.*, *22*, 3197–3212. https://doi.org/10.5194/hess-22-3197-2018.

Driedonks, A. (1982). Sensitivity analysis of the equations for a convective mixed layer. *Bound.-Layer Meteorol.*, *22*, 475–480. https://doi.org/10.1007/BF00124706.

ECMWF. (2016). *Ifs documentation cy43r1 - part iv: Physical processes*. European Centre for Medium-Range Weather Forecasts. https://doi.org/10.21957/sqvo5yxja.

Garratt, J. (1992). *The atmospheric boundary layer*. Cambridge University Press.

Gentine, P., Entekhabi, D., Chehbouni, A., Boulet, G., & Duchemin, B. (2007). Analysis of evaporative fraction diurnal behaviour. *Agric. For. Meteorol.*, *143*(1-2), 13–29. https://doi.org/10.1016/j.agrformet.2006.11.002.

Held, I. M., Hemler, R. S., & Ramaswamy, V. (1993). Radiative-convective equilibrium with explicit two-dimensional moist convection. *J. Atmos. Sci.*, *50*(23), 3909–3927. https://doi.org/10.1175/1520-0469(1993)050<3909:RCEWET>2.0.CO;2.

Khairoutdinov, M. F., & Randall, D. A. (2003). Cloud resolving modeling of the arm summer 1997 iop: Model formulation, results, uncertainties, and sensitivities. *J. Atmos. Sci.*, *60*(4), 607–625. https://doi.org/10.1175/1520-0469(2003)060<0607:CRMOTA>2.0.CO;2.

Kiehl, J., Hack, J., Bonan, G., Boville, B., Williamson, D., & Rasch, P. (1998). The national center for atmospheric research community climate model: Ccm3. *J. Clim.*, *11*(6), 1131–1149. https://doi.org/10.1175/1520-0442(1998)011<1131:TNCFAR>2.0.CO;2.

Koster, R. D., Guo, Z., Yang, R., Dirmeyer, P. A., Mitchell, K., & Puma, M. J. (2009). On the nature of soil moisture in land surface models. *Journal of Climate*, *22*(16), 4322–4335. https://doi.org/10.1175/2009JCLI2832.1.

Koster, R. D., & Mahanama, S. P. (2012). Land surface controls on hydroclimatic means and variability. *J. Hydrometeorol.*, *13*(5), 1604–1620.

Lee, J. M., & Khairoutdinov, M. (2015). A simplified land model (slm) for use in cloud-resolving models: Formulation and evaluation. *J. Adv. Model. Earth Syst.*, *7*(3), 1368–1392. https://doi.org/10.1002/2014MS000419.

Manabe, S., & Strickler, R. F. (1964). Thermal equilibrium of the atmosphere with a convective adjustment. *J. Atmos. Sci.*, *21*(4), 361–385. https://doi.org/10.1175/1520-0469(1964)021<0361:TEOTAW>2.0.CO;2.

Milly, P. C., & Dunne, K. A. (2016). Potential evapotranspiration and continental drying. *Nat. Clim. Change*, *6*(10), 946–949. https://doi.org/10.1038/nclimate3046.

Miyawaki, O., Shaw, T. A., & Jansen, M. F. (2022). Quantifying energy balance regimes in the modern climate, their link to lapse rate regimes, and their response to warming. *J. Clim.*, *35*(3), 1045–1061. https://doi.org/10.1175/JCLI-D-21-0440.1.

Monin, A., & Obukhov, A. (1954). Basic laws of turbulent mixing in the surface layer of the atmosphere. *Contrib. Geophys. Inst. Acad. Sci. USSR*, *151*(163), e187.

Porporato, A. (2009). Atmospheric boundary-layer dynamics with constant bowen ratio. *Bound.-Layer Meteorol.*, *132*, 227–240. https://doi.org/10.1007/s10546-009-9400-8.

Raymond, D. J., & Zeng, X. (2005). Modelling tropical atmospheric convection in the context of the weak temperature gradient approximation. *Quart. J. Roy. Meteor. Soc.*, *131*(608), 1301–1320. https://doi.org/10.1256/qj.03.97.

Scheff, J., & Frierson, D. M. (2015). Terrestrial aridity and its response to greenhouse warming across cmip5 climate models. *J. Clim.*, *28*(14), 5583–5600. https://doi.org/10.1175/JCLI-D-14-00480.1.

Seneviratne, S. I., Corti, T., Davin, E. L., Hirschi, M., Jaeger, E. B., Lehner, I., ... Teuling, A. J. (2010, May). Investigating soil moisture–climate interactions in a changing climate: A review. *Earth-Sci. Rev.*, *99*(3-4), 125–161. https://doi.org/10.1016/j.earscirev.2010.02.004.

Sobel, A. H., Nilsson, J., & Polvani, L. M. (2001). The weak temperature gradient approximation and balanced tropical moisture waves. *J. Atmos. Sci.*, *58*(23), 3650–3665. https://doi.org/10.1175/1520-0469(2001)058<3650:TWTGAA>2.0.CO;2.

Stahl, M. O., & McColl, K. A. (2022). The seasonal cycle of surface soil moisture. *J. Clim.*, *35*(15), 4997–5012. https://doi.org/10.1175/JCLI-D-21-0780.1.

Tennekes, H. (1973). A model for the dynamics of the inversion above a convective boundary layer. *J. Atmos. Sci.*, *30*(4), 558–567. https://doi.org/10.1175/1520-0469(1973)030<0558:AMFTDO>2.0.CO;2.